

Modeling power and linewidth of quantum dot superluminescent light emitting diode

Cite as: J. Appl. Phys. **128**, 083102 (2020); <https://doi.org/10.1063/1.5131550>

Submitted: 17 October 2019 . Accepted: 07 August 2020 . Published Online: 25 August 2020

Shampa Guin , and Nikhil Ranjan Das 



View Online



Export Citation



CrossMark

Lock-in Amplifiers
up to 600 MHz



Modeling power and linewidth of quantum dot superluminescent light emitting diode

Cite as: J. Appl. Phys. 128, 083102 (2020); doi: 10.1063/1.5131550

Submitted: 17 October 2019 · Accepted: 7 August 2020 ·

Published Online: 25 August 2020



View Online



Export Citation



CrossMark

Shampa Guin^{a)}  and Nikhil Ranjan Das^{b)} 

AFFILIATIONS

Institute of Radio Physics and Electronics, University of Calcutta, 92, Acharya Prafulla Chandra Road, Kolkata 700009, West Bengal, India

^{a)}shampaphysics@gmail.com

^{b)}Author to whom correspondence should be addressed: nrd@ieee.org. Telephone: +91 33 23509115. Fax: +91 33 23515828

ABSTRACT

A model for quantum dot (QD) superluminescent light emitting diode (SLED) is presented to study an optical power output and linewidth over a wide range of injection currents. The analysis is based on the photon and carrier rate equations including the effects of homogeneous and inhomogeneous broadening, carrier escape process, and high-current heating. The model is validated using experimental data available from the literature. The results show non-monotonic variations of the output optical power and linewidth of the SLED with the injection current density. It is seen that there exists an optimum injection current density for which the power–linewidth product becomes maximum for a given device length of the QD SLED.

Published under license by AIP Publishing. <https://doi.org/10.1063/1.5131550>

I. INTRODUCTION

The advantage of the high power of laser and broad linewidth (LW) of the conventional light-emitting diode (LED) can be implemented simultaneously using superluminescent light emitting diodes (SLEDs). This makes it suitable for some important applications, such as sub-cellular imaging, structural health monitoring, laser spectroscopy, ghost imaging, etc., to satisfy the requirement of high resolution and large probing depth for such applications.^{1–4} Quantum dot (QD) is particularly attractive in an active layer of SLED because of its advantageous characteristics arising out of complete carrier confinement in all directions. It offers higher luminescent efficiency, material gain, and has the potential for high-speed modulation even at high temperatures.^{5,6} Besides, the density of states (DOS) of the ensemble of QDs grown by the Stranski–Krastanov (SK) method deviates from an ideal delta function due to the variation in sizes of different dots.⁷ This results in inhomogeneous broadening of the output spectra, which is advantageous for certain applications, such as optical coherence tomography (OCT) for skin imaging, fiber-optic interferometer, etc.,^{8,9} where a broad linewidth of a high-power optical source is required for higher resolutions. High performance of a device depends on its good design which demands a representative physics-based model. Some theoretical studies^{10–14} are reported in the literature

that study the output power and linewidth of SLEDs. However, these models have applicability over a limited range of injection current, particularly for CW operation desired for certain applications. In this paper, a detailed and systematic analysis of the power output and linewidth of QD-based SLEDs is presented, which can be applied over a wide range of injected current density for both CW and pulsed operations. The theoretical background is given in Sec. II.

II. THEORETICAL BACKGROUND

Let us consider the schematic layer structure of a QD SLED in the xz -plane shown in Fig. 1 using an InAs/GaAs QD active region as an example. The active region consists of alternate layers of an InAs QD ensemble separated by GaAs barriers. Wide gap $\text{Al}_{0.3}\text{Ga}_{0.7}\text{As}$ layers on both sides of the active region serve as the guiding layers. The dots and guiding layers are assumed doped and barriers undoped in the computations. Dots are assumed self-assembled grown by the Stranski–Krastanov method. The contact and buffer layers are as shown in the figure. The model presented here for QD SLED is, however, general and applies to different materials and structure parameters. The input current is injected along the x -direction for the bias applied between the top and bottom contacts. The structure is assumed to be homogeneous

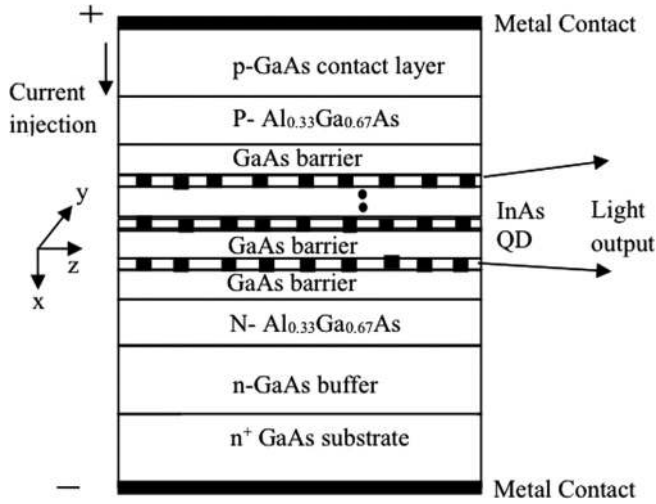


FIG. 1. Schematic structure of the QD SLED structure. The materials of different layers are shown taking example of an InAs/GaAs QD active region.

along the y -direction, so current spreading effect is neglected in the analysis. Photons generated within the active region travel along the z axis. Now, the rate equations are solved to find the relationship between the injected carriers and the generated photons in the SLED.^{15,16}

The photon rate equations, under steady state conditions, for SLEDs with QDs in the active layer, can be written as follows:

$$v_{ph} \frac{dN_{pf,i}(\langle n \rangle, E, z)}{dz} = v_{ph} \{ \Gamma g_{m,i}(\langle n \rangle, E) - \alpha \} N_{pf,i}(\langle n \rangle, E, z) + \delta_f R_{sp,i} - \frac{N_{pf,i}}{\tau_p} \quad (1)$$

for forward propagating waves (+ z direction) and

$$v_{ph} \frac{dN_{pb,i}(\langle n \rangle, E, z)}{dz} = -v_{ph} \{ \Gamma g_{m,i}(\langle n \rangle, E) - \alpha \} N_{pb,i}(\langle n \rangle, E, z) - \delta_b R_{sp,i} - \frac{N_{pb,i}}{\tau_p} \quad (2)$$

for backward propagating waves ($-z$ direction).

Subscripts f and b represent the forward and backward directions, respectively, $N_{pf,i}$ ($N_{pb,i}$) is forward (backward) traveling photon densities in the i th QD layer at z having energy E , $\langle n \rangle$ is the average number of electron hole pairs per QD, Γ is the confinement factor, α is the optical loss in the active material, v_{ph} is the photon velocity within the active region, τ_p is the photon lifetime which takes into account the photons lost from the cavity, such as escape of photons from end facets, absorption in cavity (excluding the active region). Symbol δ_f (δ_b) is used to denote the fraction of the spontaneous emission contributed to the photons propagating in the forward (backward) direction.¹⁷

The active region of this SLED consists of several QD-layers separated by barrier layers. Each of these QD-layers is an ensemble

of quantum dots grown by the SK method, as mentioned earlier. The dots in each layer differ randomly in size and shape. Taken together, this inhomogeneity of dots results in a spread of energy states around a nominal value, where the density of states follows the Gaussian distribution. So, the effect of all dots in a layer can be taken into account by assuming an equivalent single dot structure with in-homogeneously broadened distribution of states. Thus, the material gain of this equivalent single dot structure is estimated avoiding the complexity of calculating gains separately from all individual dots in a layer.

The material gain $g_{m,i}(\langle n \rangle, E)$ of the i th QD-layer of the SLED at energy E is derived from the calculation of emission and absorption rates based on Fermi's golden rule and is given by¹⁶

$$g_{m,i}(\langle n \rangle, E) = \frac{2\pi e^2 N_D}{c n_r \epsilon_0 m_0^2} \sum_{c,v} \frac{|P_{cv,i}|^2}{\omega_{cv,i}} \times \int_{-\infty}^{+\infty} \{ f_c(E') - f_v(E') \} B_0(E' - E_{cv,i}) B_{cv}(E - E') dE', \quad (3)$$

where $f_v(E')$ and $f_c(E')$ are Fermi occupation probabilities of electrons in the valence band and conduction band, respectively, $\omega_{cv,i}$ is the frequency of emitted light, $P_{cv,i}$ is the momentum matrix element, $E_{cv,i}$ is the transition energy, which is a sum of the electron energy, hole energy, and bandgap energy, subscript i is used to include the variable/parameter in the i th dot layer, n_r is the refractive index of the QD material, and N_D is the QD volume density. It may be noted that the factor $B_0(E'E_{cv,i})$ represents the Gaussian distribution¹⁶ of the density of energy states in the i th QD-layer to take into account the inhomogeneity of dots in that layer. In addition, the factor $B_{cv}(E-E')$ is also used to include the effect of homogeneous broadening due to the temperature variation, etc. and is usually represented by the Lorentzian line shape function.¹⁴

The carrier energies in QDs are calculated by solving the Schrödinger equation knowing the electric fields in different QD-layers as schematically shown in Fig. 2(a). The calculation of electric field at different boundaries/interfaces of the structure is given in Appendix A. These field dependent energies are further used to find the wave functions and the overlapping between the wave functions of the carriers within the QD.^{18,19} The spontaneous emission rate, $R_{sp,i}$ from the QDs in the i th dot layer is calculated from the spontaneous emission lifetime of the carriers within dots in that layer and following,²⁰ it may be written as

$$R_{sp,i}(\langle n \rangle, E) = \langle n \rangle N_D \frac{e^2 n_r}{\pi \epsilon_0 m_0^2 c^3 \hbar} \sum_{c,v} \omega_{cv,i} |P_{cv,i}|^2 \times \int_{-\infty}^{+\infty} f_c(E') [1 - f_v(E')] B_0(E' - E_{cv,i}) B_{cv}(E - E') dE'. \quad (4)$$

To develop the carrier rate equation, the physical processes considered are described below. The injected carriers get confined in the dots of the first layer of QDs due to the potential barrier between dots and barriers—a fraction of which gets recombined either radiatively or non-radiatively within the dots, and the

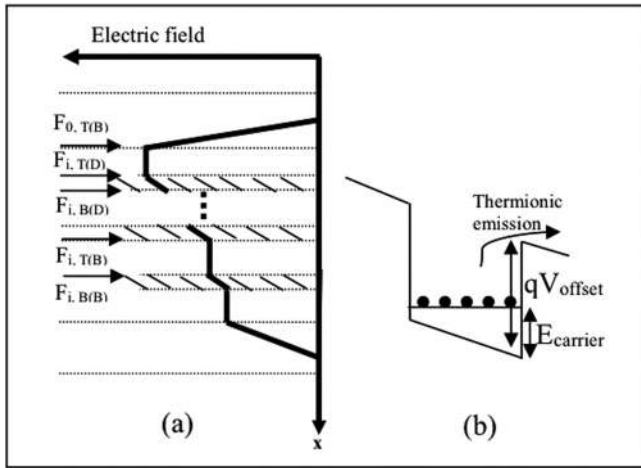


FIG. 2. (a) Schematic electric field profile across the active layer. First index of the electric field (F) symbol represents the dot layer number, second index represents top or bottom of that particular layer and last index represents dot (D) or barrier (B) layer, (b) diagram showing the effective potential barrier for thermionic emission in the presence of an electric field.

remaining fraction escapes the dots through the thermionic emission over the barrier to reach the next layer of QDs. This process continues for all the layers of the active region.

The radiative recombination within the dots is taken into account through the term $R_{sp,i}$ for the i th layer as given in (3), while the non-radiative recombination is assumed to be of the Shockley Read Hall (SRH) type and is denoted by $R_{non,i}$.

To incorporate the carrier escape process from QDs, let us consider Fig. 2(b), where qV_{offset} is the band offset between the QD and barrier, $E_{carrier}$ is the confined energy in QDs. The energy states within the dot are lowered due to the band-tilting in the presence of the applied bias. As a result, the effective potential barrier for the carriers within the dot is changed to $(qV_{offset} - E_{carrier})$. So, following Refs. 21,22, the carrier loss rate due to escape of carriers from dots in the i th layer may be written as

$$R_{emi,i} = B e^{\left(\frac{qV_{offset} - E_{carrier,i}}{kT}\right)}, \quad (5)$$

where B is a material dependent constant and assumed to be the same for both electrons and holes.

When the injection current is high, the heating effect reduces the number of available carriers for radiative recombination. The generated heat is equated to the kinetic energy of the carriers to calculate the amount of heating per unit volume per unit time and is given by $2\rho C_f^2 J^2 / m_e v_d^2$, where J is the injected current density, C_f is the fraction of J responsible for generation of heat, v_d , m_e , and ρ are, respectively, the thermal velocity, effective mass of the carriers within QDs, and resistivity. The overall effective resistivity may be approximately written as $\rho = \sum_k \rho_k d_k / \sum_k d_k$, assuming the same area and uniform resistivity in each layer (k) of thickness d_k in the structure,

$$\frac{J}{q d_{QD} N_{QD}} - C_f^2 \frac{2J^2 \rho}{m_e v_d^2} = \sum_i \left[\int_{-\infty}^{+\infty} \{v_{ph} [\Gamma g_{m,i}(\langle n \rangle, E) - \alpha] [N_{pf,i}(\langle n \rangle, E) + N_{pb,i}(\langle n \rangle, E)] + R_{sp,i}\} dE + R_{non,i} + R_{emi,i} \right], \quad (6)$$

where d_{QD} and N_{QD} are the dot height and layer number of QDs, respectively. The first term on the right side of (5) represents the loss of carriers due to stimulated emission. The summation is taken over the number of QD layers (i) to obtain the total emissions from all the QD layers. It may be noted that the photon densities used in (5) are averaged over the length of the device.

Now, the rate equations (1) and (5) are solved self-consistently to find the photon and carrier distribution within the device. The computation is done numerically as shown in the flow chart given in Appendix B. The solution is obtained for a constant injection current density across the contact region assuming no current spreading and by using appropriate boundary conditions at the end facets. The solution, $\langle n \rangle$, obtained from the iterative method, is used to find the distribution of forward and backward traveling photon densities at z in the i th dot layer as follows:

$$N_{pf,i}(\langle n \rangle, z, E) = N_{f0,i} e^{g_i \left(1 - \frac{1}{g_i v_{ph} \tau_p}\right) z} + \frac{N_{spf,i}}{1 - \frac{1}{g_i v_{ph} \tau_p}} \left(e^{g_i \left(1 - \frac{1}{g_i v_{ph} \tau_p}\right) z} - 1 \right), \quad (7)$$

$$N_{pb,i}(\langle n \rangle, z, E) = N_{b0,i} e^{-g_i \left(1 - \frac{1}{g_i v_{ph} \tau_p}\right) z} + \frac{N_{spb,i}}{1 - \frac{1}{g_i v_{ph} \tau_p}} \left(e^{-g_i \left(1 - \frac{1}{g_i v_{ph} \tau_p}\right) z} - 1 \right), \quad (8)$$

where g_i is the modal gain (assumed uniform along z), $N_{f0,i}$ ($N_{b0,i}$) is the forward (backward) traveling photon densities at $z = 0$ and $N_{spf,i}$ ($N_{spb,i}$) is the forward (backward) photon densities generated from the spontaneous emission of the i th QD layer. The above generalized analysis is applicable for devices also having optical input in addition to the injected currents. Assuming no optical input, as is usual in the case of a SLED (i.e., $N_{f0,i} = N_{b0,i} = R_0$), the photon density at the output facet (on the right in Fig. 1) from the i th layer, $N_{pL,i}$ is derived using Eqs. (6) and (7) as

$$N_{pL,i}(E) = \frac{\{e^{g_i(1-1/g_i v_{ph} \tau_p)L} - 1\} \left\{ \frac{N_{spf,i}}{(1-1/g_i v_{ph} \tau_p)} + e^{g_i(1-1/g_i v_{ph} \tau_p)L} N_{spf,i} R_0 \right\}}{1 - R_0 R_L e^{2g_i(1-1/g_i v_{ph} \tau_p)L}}, \quad (9)$$

where L is the length of the active layer, R_0 , R_L are the input and output facet reflectivities, respectively. So, the optical power spectral density (PSD), $P_\lambda(E)$, is obtained from the following expression:

$$P_\lambda(E) = (1 - R_L) v_{ph} w d_{QD} h c \sum_i N_{pLi}(E) / \lambda, \quad (10)$$

where w is the width of the active layer and the summation is used over all the dot layers. The above PSD is integrated over photon energy (E), where the gain profile [Eq. (2)] holds to obtain optical power output.

III. RESULTS AND DISCUSSIONS

Using the equations given earlier, the computations are done taking InAs/GaAs QD SLED as an example. The computational approach is described through a flow chart in Appendix B. First, the output power is computed to compare with experimental data taken from the literature. The nominal dot heights in QD-layers and barrier thicknesses are kept same as used in many studies.^{5,23–25} However, to the knowledge of the authors, a suitable experimental report with a similar structure and for cw operation at high current is not available in the literature to verify the model. So, the authors chose Ref. 26 of the same material system, where an experimental result for cw operation over a wide range of current density was found suitable for comparing models, though it²⁶ used a special structure with variable dot heights in different QD-layers and variable cap layer thicknesses for the purpose of increasing linewidth. To replace this structure with an equivalent structure as used in the model, the central wavelength of an output spectrum (1033 nm²⁶) is taken as the common reference and that needed nominal dot heights to be 5 nm in all QD-layers, keeping other parameters such as barrier thickness (30 nm) separating QD layers, dot density, number of dot layers, facet reflectivities, etc. the same as in Ref. 26. Other material parameters, if any, not found in Ref. 26 are taken from references given in Table I. It may be noted that heights of SK-grown QDs in a particular layer also vary in size. So, the choice of an equivalent nominal height may be considered reasonable. The model results and experimental data are now plotted as a function of injection current density in Fig. 3 for a 1 mm device length. The plot shows reasonably good agreement in the nature of the model output with experimental data over the

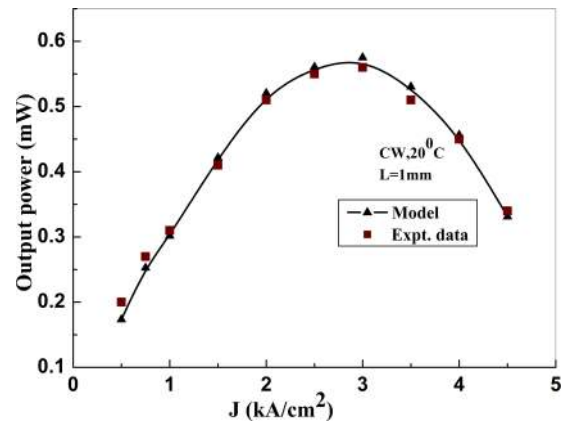


FIG. 3. Comparison of the output power obtained from the model with the experimental data taken from the literature²⁶ for a device length of 1 mm.

entire range of the current density. It may be mentioned here that the extrinsic (parasitic) effect due to different layers may appear through an equivalent series resistance. But, this series resistance does not affect the current density (steady-state) dependent plot, except a contribution to heating (at high current through contribution to overall effective resistivity, ρ) as included in the model.

The model is now used to obtain the subsequent results based on computations taking the following values of parameters as an example. The structure has four layers of InAs QD having a nominal height of 5 nm, a doping density of 10^{18} cm^{-3} separated by 20 nm undoped GaAs barriers, a dot density of $5 \times 10^{10} \text{ cm}^{-2}$, an aperture width of $35.49 \mu\text{m}$, and a device length of 1 mm unless otherwise specified. Besides, zero facet reflectivity and confinement factor of 0.1 are assumed. The material parameters used in subsequent simulations are given in Table I.

TABLE I. Material parameters used for the SLED structure.

| Parameter | Value used in the analysis |
|-----------------------------------|---------------------------------------|
| InAs/GaAs CB offset ²⁷ | 0.55 eV |
| InAs/GaAs VB offset ²⁷ | 0.35 eV |
| Bandgap ²⁷ | 0.524 eV (including effect of strain) |
| Refractive index ²⁸ | 3.51 |
| Thermal velocity ²⁸ | $7.7 \times 10^{10} \text{ ms}^{-1}$ |
| Material loss ²⁹ | 2 cm^{-1} |
| Photon lifetime ²⁹ | 8.3 ps |

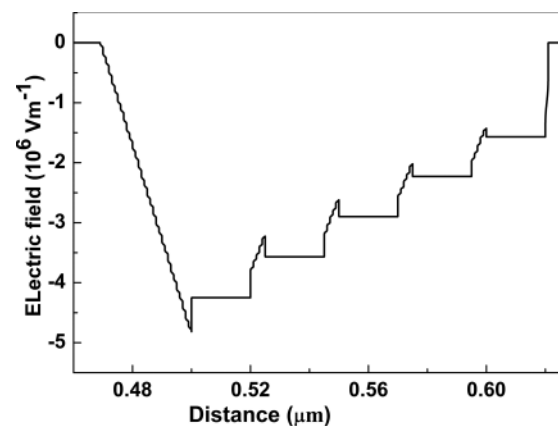


FIG. 4. Variation of the electric field within the QD, barrier, and cladding layer.

The electric field at different regions within the SLED is obtained using the calculations shown in Appendix A and is plotted as a function of distance in Fig. 4. It is seen that electric field varies linearly within the QD, while it remains the same in the undoped barrier. It may be noted that each dot layer has different electric fields, which contributes to peak gain at different wavelengths. This information is used in the calculation of photon density from different dot layers using (8). Then, (9) is used to find the output power spectra (PSD) and total output power from SLED.

The nature of variation of power with current density (as in Fig. 3) shows that, for low current densities, the output power increases with the injection current density. This happens because of the availability of more carriers within the dots due to confinement and hence, radiative recombination increases within the dot. As the current density is increased above a certain value, the heat generation within the device becomes significant, which reduces the effective number of carriers available for radiative recombination, thus reducing the output optical power. In this computation, B and C_f are taken as $2.65 \times 10^{12}/s$ and 4.75×10^{-3} , respectively, and are kept same throughout the analysis. This variation of average number of carriers within dot, $\langle n \rangle$, is shown using dotted lines in Fig. 5. It is seen from the plot (red dotted line) that $\langle n \rangle$ initially increases for low current densities and after attaining a peak value it decreases. This decrease in the output power at high current density is, however, not seen if the heating effect is not considered as shown in that figure (dashed and solid lines). Also, the effect of escape of carriers on output power is seen very small (comparing solid and dashed lines). This variation of $\langle n \rangle$ modifies the modal gain, which is plotted in Fig. 6 for different injected current densities. It can be noted that the modal gain is negative for a low current density due to the availability of less carriers for radiative recombination. As the injection current density increases, the modal gain becomes positive and after attaining a maximum value, it decreases. This happens because of the reduction in the effective number of carriers available for radiative recombination,

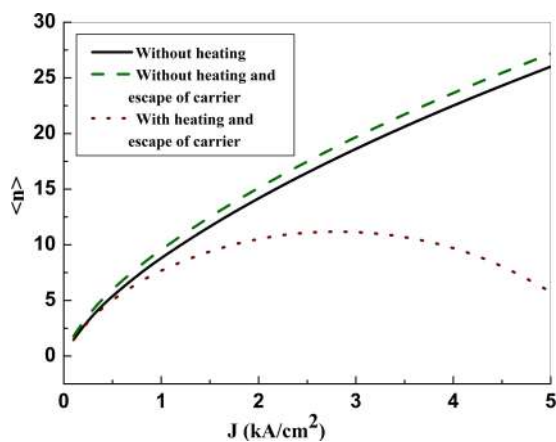


FIG. 5. Variation of the average number of carriers per QD, $\langle n \rangle$ for 1 kA cm^{-2} injected current density.

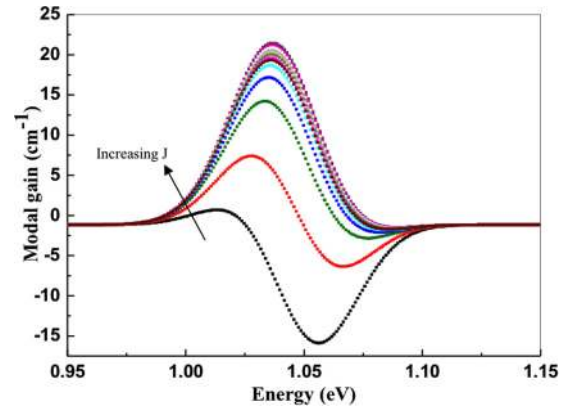


FIG. 6. Variation of the modal gain for input current densities starting from 100 A/cm^2 to 5 kA/cm^2 at the step of 250 A/cm^2 for 1 mm .

as shown in Fig. 5. This influences the density of photons generated from dot layers.

The spectral distribution of the photon densities from different QD layers along with the overall spectral distribution is shown in Fig. 7. The results are shown for photon densities normalized to their peak values. It may be noted that the photons emitting from each dot layer have different transition energies (mean of Gaussian distribution) due to the different electric fields developed in each dot layer for the applied bias. Thus, there is a shift in the mean of Gaussian distribution from one QD layer to the other. So, the overlap of the distribution function from different layers results in an increase in the overall broadening, and the power output has a broader linewidth than the individual spectrum from each QD layer. Since the total photon density is the sum of photon densities from each dot layer, the overall spectral density of the power output has a broader linewidth than the individual spectrum from each

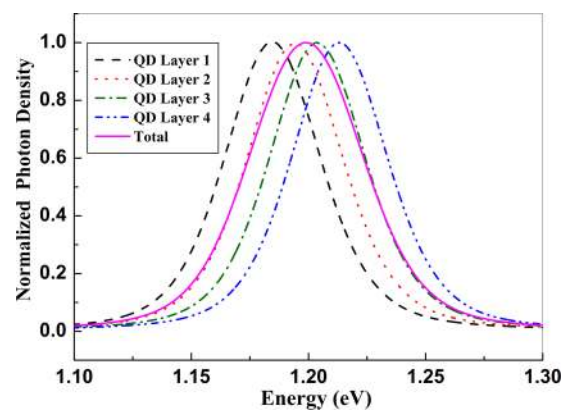


FIG. 7. Variation of the normalized photon densities at output facets from each QD layer for a 1 mm device length and 1 kA/cm^2 injection current density (variance of dot size distribution, σ , 20 meV).

QD layer as shown in Fig. 7. It was seen¹⁸ that as the electric field increases, the emission coefficient increases while the absorption coefficient decreases, which indicates that the material gain (difference between emission and absorption coefficients) increases with the electric field. Hence, the photons generated in a dot layer get amplified according to the material gain in that particular dot layer. The optical signal at the output facet (output power) is the contribution by the photons from different layers. Figure 8 shows the variation of the output power spectra (PSD) for different current densities. The peak of PSD initially increases with injection current for lower current densities due to the increased number of carriers available for radiative recombination and then decreases due to heat dissipation at higher injection current densities as discussed earlier.

Another important the SLED parameter is its linewidth (LW), i.e., full width at half maximum (FWHM) which is plotted in Fig. 9 as a function of injection current density for different device lengths. It is seen that, as the injection current density increases, the FWHM first decreases, reaches a minimum, and then increases. This is due to the reason given below. At low and high injection currents, the carriers available for radiative recombination are small as shown in Fig. 5, which is responsible for a low material gain. As a result, the stimulated emission rate reduces making the spontaneous emission more dominant to broaden the output spectra at low and high injection currents.

From the previous discussions, it is seen that the output optical power and FWHM change in opposite directions as current density is increased. However, when both power and linewidth are important, the power (P)–FWHM (LW) product (say, PLW) may be considered as a useful performance criterion. So, PLW is plotted in Fig. 10 as a function of injected current densities for different device lengths. The plot suggests that there exists an optimum current density for a given length, for which the product becomes maximum. It may be mentioned here that in obtaining this plot the

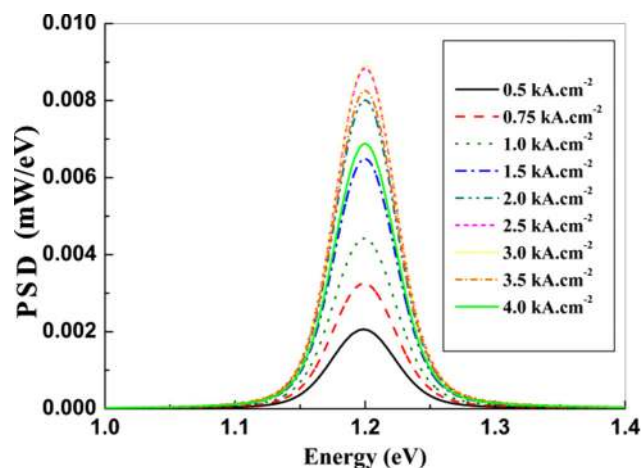


FIG. 8. Variation of the output power spectra (PSD) for different current densities at a 1 mm device length. The overall emission wavelength is around 1033 nm having a linewidth of 50.35 nm at 1 kA/cm².

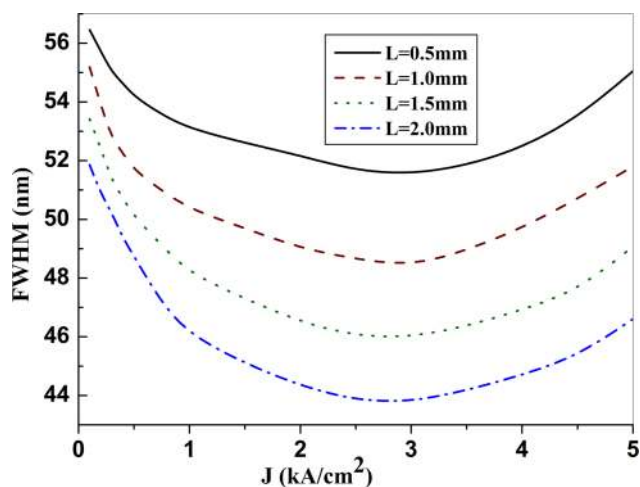


FIG. 9. Variation of FWHM, with current density for different device lengths.

model parameters for different device lengths are kept fixed as a reasonable approximation. Any possible small variation of these parameters may change the output a little, but the inference on the existence of an optimum current density for the maximum PLW of the QD SLED remains unchanged.

A summary of the optimum design and maximum PLW is given in Table II for different device lengths. The table also shows the LW (FWHM) and output power corresponding to the maximum PLW. The optimum J is extracted after smooth fitting of data. It shows that the optimum current density is less for larger lengths of the device and also provides a higher output power at the cost of FWHM. This may be a useful guide in the design of SLED for target applications.

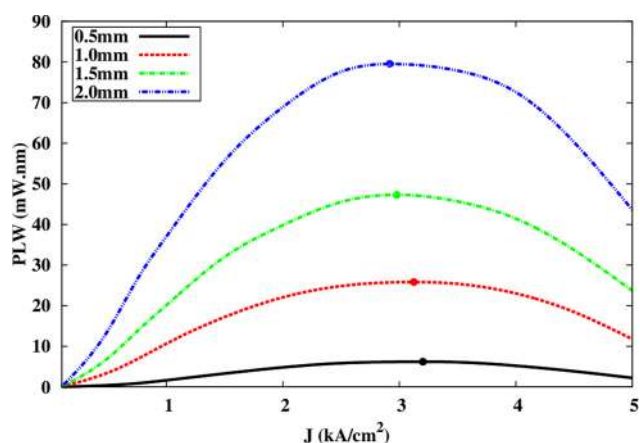
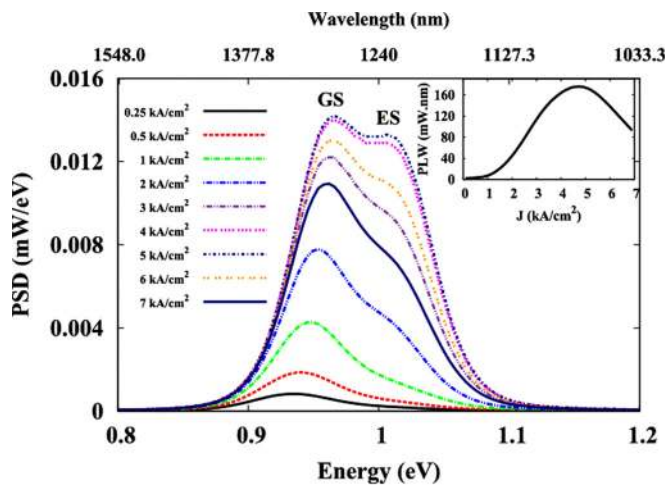


FIG. 10. Variation of the power–linewidth product (PLW) with current density for different device lengths. Dot symbols on plots indicate the maximum PLW.

TABLE II. Optimum J for the maximum PLW and other related parameters at the maximum PLW for different lengths of the device.

| Length (mm) | Optimum J (kA/cm ²) | Maximum PLW (mW nm) | LW (nm) | Output power (mW) |
|-------------|-----------------------------------|---------------------|---------|-------------------|
| 0.5 | 3.20 | 6.20 | 51.53 | 0.12 |
| 1.0 | 3.12 | 25.71 | 48.41 | 0.53 |
| 1.5 | 2.98 | 47.30 | 45.98 | 1.03 |
| 2.0 | 2.92 | 79.50 | 43.77 | 1.82 |
| 2.5 | 2.85 | 136.63 | 40.20 | 3.40 |
| 3.0 | 2.74 | 260.46 | 37.90 | 6.87 |
| 3.5 | 2.66 | 449.38 | 35.26 | 12.74 |
| 4.0 | 2.56 | 818.83 | 33.63 | 24.35 |

As it is shown in the literature, one approach to increase the linewidth (FWHM) is to use the excited state (ES) along with the ground state (GS). This, however, depends on the proximity of the states (ground state and excited state) and inhomogeneous broadening due to dot size variations in the ensemble of quantum dots. The present model may be applied to consider excited state (s) also. A plot is given in Fig. 11 using the model to show the effect of an excited state using different dot structures and other parameters as mentioned in the caption of the figure. The figure shows that as the injection current increases, the excited state is gradually occupied, resulting in broadening of the FWHM. In the inset, the variation of the power–FWHM product with current density is shown, which shows the existence of the optimum current density for the maximum power–FWHM product. It may be noted here that in the case of structures with the excited state,

**FIG. 11.** Output optical power spectra (PSD) of a SLED structure for different current densities in the presence of an excited state. Dot size ($3 \times 20 \times 20 \text{ nm}^3$), barrier thickness 30 nm, σ 30 meV, device length 1 mm, other parameters remaining the same as before. The inset shows the variation of the power–FWHM product.

the electron escape mechanism from dots mentioned earlier is a partial picture. There is an additional possibility of a two-step escape mechanism in the presence of an excited state: transition (thermal) of electrons from the ground state to the excited state followed by tunneling through a triangular barrier. This probability is, however, very low for an occupied excited state and thick barrier. In this case, the thermionic emission from the occupied excited state [as in (4)] may be relatively significant among the possible escape processes. Also, the effect of escape is seen (Fig. 5) very small compared to other dominant physical processes shown in the model. So, the model may predict the output reasonably well.

IV. CONCLUSION

The output optical power and linewidth of QD SLED are studied over a wide range of injection current by solving steady state carrier and photon rate equations. The model includes the effects of homogeneous and inhomogeneous broadenings, escape of carriers from QD, heat dissipation at high injection, etc. To solve the steady state rate equations, the modal gain and spontaneous emission rate are calculated using Fermi's golden rule and knowing the electric fields at different interfaces of the quantum dot active layer. The model is validated taking experimental data from the literature. The results show the variation of output optical power and linewidth with injection current for different device lengths. As the injection current increases, the output power increases reaching a maximum and then decreases. This reduction in the optical power at a high injection current density is due to the reduction in the material gain of the quantum dots. The physical mechanism behind the reduction of the material gain is the heat generation at a high injection current density, which reduces the effective number of carriers available for radiative recombination within the dot. The linewidth initially decreases, reaches a minimum, and then increases with the injection current density. This is because, at low and high injection levels, the modal gain is small and, hence, the spontaneous emission becomes more significant than stimulated emission. As a result, the linewidth increases for both low and high injection levels. It is seen that power and linewidth varies in opposite directions. Besides, there exists an optimum injection current density for the maximum power–linewidth product of the QD SLED for a given device length. This makes QD SLEDs an important source for sub-cellular imaging, where high powers and large linewidths are desired.

ACKNOWLEDGMENTS

The authors wish to acknowledge the help received from the colleagues in their research group at different times during the course of the work. The authors also acknowledge Dr. Jayanta Sarma, University of Bath, U.K., for his valuable suggestions regarding SLED modeling. The partial financial support from the U.K. India Education and Research Initiative (UKIERI) programme (No. UKUTP201100253) at the beginning of the work is also thankfully acknowledged.

APPENDIX A: ELECTRIC FIELD DISTRIBUTION IN THE STRUCTURE

A schematic electric field profile is shown in Fig. 2(a). To calculate the electric field and potential profiles within the QD and the barrier, Poisson's equation is solved. In the following, the electric fields at different boundaries are expressed in terms of the electric field at the top of first barrier after the p-cladding layer, $F_{0,T(B)}$. Then, the electric field at the top of the barrier of the i th dot layer is given by

$$F_{i,T(B)} = F_{0,T(B)} - i \frac{qn_{dot}d_{QD}}{\epsilon_2}, \quad (A1)$$

where n_{dot} is the carrier density within dots, ϵ_1 is the permittivity of QDs, and ϵ_2 is the permittivity of the barrier. The electric field at the bottom of the barrier, $F_{i,B(B)}$ of the i th dot layer is same as (A1). The electric fields at the top and bottom in the i th dot layer are, respectively, given as

$$F_{i,T(D)} = \frac{\epsilon_2}{\epsilon_1} F_{0,T(B)} - i \frac{qn_{dot}d_{QD}}{\epsilon_1}, \quad (A2)$$

$$F_{i,B(D)} = \frac{\epsilon_2}{\epsilon_1} F_{0,T(B)} - (i-1) \frac{qn_{dot}d_{QD}}{\epsilon_1}. \quad (A3)$$

The voltage-drop across all layers along with the built-in potential is used to calculate the total voltage-drop across the structure. For a given applied voltage, $F_{0,T(B)}$ is calculated and hence, fields at all other interfaces are calculated using equations mentioned above.

It may be mentioned here that in the above derivation a specific concentration n_{dot} is assumed, though in a rigorous calculation, it could be found using the self-consistent solution of Poisson and Schrödinger equations. Complexity is further increased with the consideration of unequal distribution and shape of dots in layers. So, we have used an approximate approach to simply the calculation assuming an average n_{dot} . However, the value of n_{dot} is found separately for each injection current density using an iterative approach. These electric fields are then used in Schrödinger equation to find the subband energies, wave functions, and the overlapping between the wave functions of the carriers within the QD.

APPENDIX B: COMPUTATIONAL APPROACH

The computational approach is described in Fig. 12 through a flow chart. Using an initial guess of $\langle n \rangle$, the electric field is calculated (Appendix A), and then energy eigenvalues and wave functions are calculated using the Schrödinger equation. Optical gain, emission rate, and different photon densities are calculated using Eqs. (2), (3), (6), and (7). These values along with other parameters are used to solve Eq. (5) iteratively to obtain $\langle n \rangle$ for the given current density (J). Finally, output photon density and optical power spectra at output facet are computed. Simulation is done running codes in MATLAB.

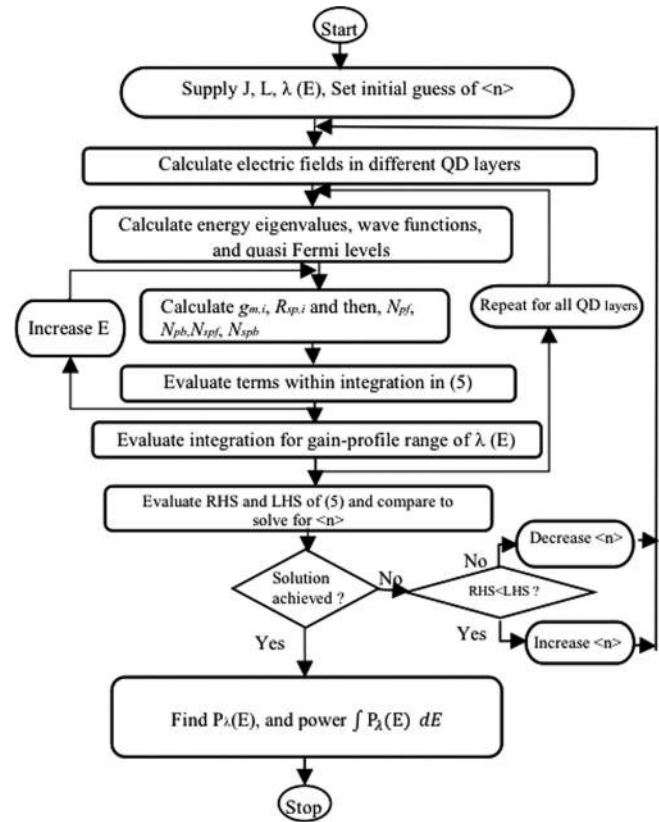


FIG. 12. Flowchart for simulation steps.

DATA AVAILABILITY

The data that support the findings of this study are available within the article.

REFERENCES

- ¹N. Krstajić, L. E. Smith, S. J. Matcher, D. T. D. Childs, M. Bonesi, P. D. L. Greenwood, M. Hugues, K. Kennedy, M. Hopkinson, K. M. Groom, S. MacNeil, R. A. Hogg, and R. Smallwood, "Quantum dot superluminescent diodes for optical coherence tomography: Skin imaging," *IEEE J. Sel. Top. Quantum Electron.* **16**(4), 748–754 (2010).
- ²S. Wei, J. Yang, F. Fan, W. Huang, D. Li, and B. Xua, "Compact quantum random number generator based on superluminescent light-emitting diodes," *Rev. Sci. Instrum.* **88**(1–5), 123115 (2017).
- ³P. Janassek, S. Blumenstein, and W. Elsaßer, "Ghost spectroscopy with classical thermal light emitted by a superluminescent diode," *Phys. Rev. Appl.* **9**(1–6), 021001 (2018).
- ⁴K. Vizbaras, E. Dvinelis, I. Simonyt, A. Trinkunas, M. Greibus, R. Songaila, T. Zukauskas, M. Kausylas, and A. Vizbaras, "High power continuous-wave GaSb-based superluminescent diodes as gain chips for widely tunable laser spectroscopy in the 1.95–2.45 μm wavelength range," *Appl. Phys. Lett.* **107**(1–4), 011103 (2015).

- ⁵Z. Y. Zhang, Z. G. Wang, B. Xu, P. Jin, Z. Z. Sun, and F. Q. Liu, "High-performance quantum-dot superluminescent diodes," *IEEE Photonics Technol. Lett.* **16**, 27–29 (2004).
- ⁶D. C. Heo, J. D. Song, W. J. Choi, J. I. Lee, J. C. Jung, and I. K. Han, "High power broadband InGaAs/GaAs quantum dot superluminescent diodes," *Electron. Lett.* **39**(11), 863–865 (2003).
- ⁷J. X. Chen, A. Markus, A. Fiore, U. Oesterle, R. P. Stanley, J. F. Carlin, R. Houdré, and M. Ilegems, "Tuning InAs/GaAs quantum dot properties under Stranski-Krastanov growth mode for 1.3 μm applications," *J. Appl. Phys.* **91**, 6710 (2002).
- ⁸S. K. Ray, T. L. Choi, K. M. Groom, B. J. Stevens, H. Liu, M. Hopkinson, and R. A. Hogg, "High-power and broadband quantum dot superluminescent diodes centered at 1250 nm for optical coherence tomography," *IEEE J. Sel. Top. Quantum Electron.* **13**(5), 1267–1272 (2007).
- ⁹Y. N. Ning, K. T. V. Grattan, and A. W. Palmer, "Fibre-optic interferometric systems using low-coherence light sources," *Sens. Actuators A* **30**, 181–192 (1992).
- ¹⁰M. T. Crowley, N. Patel, T. A. Saiz, M. E. Emawy, T. A. Nilsen, N. A. Naderi, S. D. Mukherjee, B. O. Fimland, and L. F. Lester, "Modelling the spectral emission of multi-section quantum dot superluminescent light-emitting diodes," *Semicond. Sci. Technol.* **27**(1–5), 065011 (2012).
- ¹¹M. Rossetti, L. Li, A. Markus, A. Fiore, L. Occhi, C. Velez, S. Mikhrin, I. Krestnikov, and A. Kovsh, "Characterization and modeling of broadband spectrum InAs-GaAs quantum dot superluminescent diodes emitting at 1.2–1.3 μm ," *IEEE J. Quantum Electron.* **43**(8), 676–686 (2007).
- ¹²N. Matuschek and M. Duell, "Modeling and simulation of superluminescent light-emitting diodes (SLEDs)," *IEEE J. Sel. Top. Quantum Electron.* **19**(5), 1 (2013).
- ¹³P. Bardella, M. Rossetti, and I. Montrosset, "Modeling of broadband chirped quantum-dot super-luminescent diodes," *IEEE J. Sel. Top. Quantum Electron.* **15**(3), 785–791 (2009).
- ¹⁴S. K. Ray, K. M. Groom, R. Alexander, K. Kennedy, H. Y. Liu, M. Hopkinson, and R. A. Hogg, "Design, growth, fabrication, and characterization of InAs/GaAs 1.3 μm quantum dot broadband superluminescent light emitting diode," *J. Appl. Phys.* **100**(1–6), 103105 (2006).
- ¹⁵J. Park and X. Li, "Theoretical and numerical analysis of superluminescent diodes," *J. Light. Technol.* **24**, 2473–2480 (2006).
- ¹⁶M. Sugawara, K. Mukai, Y. Nakata, H. Ishikawa and A. Sakamoto, "Effect of homogeneous broadening of optical gain on lasing spectra in self-assembled $\text{In}_x\text{Ga}_{1-x}\text{As}$ /GaAs quantum dot lasers," *Phys. Rev. B* **61**, 7595–7603 (2000).
- ¹⁷F. Causa and J. Sarma, "Realistic model for the output beam profile of stripe and tapered superluminescent light-emitting diodes," *Appl. Opt.* **42**(21), 4341–4348 (2003).
- ¹⁸S. Guin and N. R. Das, "Enhancement of optical gain in quantum dot ensemble with electric field," *Superlattices Microstruct.* **125**, 151–158 (2019).
- ¹⁹N. R. Das and A. N. Chakravarti, "On the electron states in a cylindrical quantum box of a wide-gap semiconductor in crossed electric and magnetic fields," *Phys. Status Solidi B* **169**, 97–104 (1992).
- ²⁰M. Sugawara, "Self-assembled InGaAs/GaAs quantum dots," in *Semiconductors and Semimetals* (Academic Press, San Diego, 1999), Vol. 60.
- ²¹N. R. Das and M. J. Deen, "Calculating the photocurrent and transit time limited bandwidth of a heterostructure p-i-n photodetector," *IEEE J. Quantum Electron.* **37**(12), 1574–1587 (2001).
- ²²M. K. Das and N. R. Das, "Calculating the responsivity of a resonant-cavity-enhanced multiple quantum well photodetector," *J. Appl. Phys.* **105**(9), 093118 (2009).
- ²³L. H. Li, M. Rossetti, A. Fiore, L. Occhi, and C. Velez, "Wide emission spectrum from superluminescent diodes with chirped quantum dot multilayers," *Electron. Lett.* **41**(1), 41–43 (2005).
- ²⁴M. Rossetti, A. Markus, A. Fiore, L. Occhi, and C. Velez, "Quantum dot superluminescent diodes emitting at 1.3 μm ," *IEEE Photonics Technol. Lett.* **17**(3), 540–542 (2005).
- ²⁵N. Ozaki, D. T. D. Childs, J. Sarma, T. S. Roberts, T. Yasuda, H. Shibata, H. Ohsato, E. Watanabe, N. Ikeda, Y. Sugimoto, and R. A. Hogg, "Superluminescent diode with a broadband gain based on self-assembled InAs quantum dots and segmented contacts for an optical coherence tomography light source," *J. Appl. Phys.* **119**(1–8), 083107 (2016).
- ²⁶S. Haffouz, P. J. Barrios, R. Normandin, D. Poitras, and Z. Lu, "Ultrawide-bandwidth, superluminescent light-emitting diodes using InAs quantum dots of tuned height," *Opt. Lett.* **37**(6), 1103–1105 (2012).
- ²⁷J. Kim and S. L. Chuang, "Theoretical and experimental study of optical gain, refractive index change, and linewidth enhancement factor of p-doped quantum-dot lasers," *IEEE J. Quantum Electron.* **42**(9), 942–952 (2006).
- ²⁸See <http://www.ioffe.ru/SVA/NSM/Semicond/InAs/> for 'refractive index' and 'thermal velocity' used in computation.
- ²⁹L. Shao-Feng, I. Montrosset, M. Gioannini, S. Shu-Zhong, and M. Jian-Wei, "Modeling and simulation of InAs/GaAs quantum dot lasers," *Optoelectron. Lett.* **7**(2), 122–125 (2011).